Chemical Engineering Journal 522 (2025) 167294

Contents lists available at ScienceDirect

Chemical Engineering Journal

journal homepage: www.elsevier.com/locate/cej

Preheating applied on a 915 MHz CO_2 microwave plasma: Unlocking the potential for heat recycling in plasma systems

E.R. Mercer [a,b,*,1], C.F.A.M. van Deursen [c,**,1], F.J.J. Peeters [c,d], W.A. Bongers [c], F.M.A. Smits [c,e], M.C.M. van de Sanden [c,f,2], A. Bogaerts [a,b,2]

[a] Research Group PLASMANT, Department of Chemistry, University of Antwerp, Universiteitsplein 1, 2610 Antwerpen, Belgium
[b] Electrification Institute, University of Antwerp, Olieweg 97, 2020 Antwerp, Belgium
[c] Research Group PSFD, Dutch Institute of Fundamental Energy Research, De Zaale 20, 5612AJ Eindhoven, the Netherlands
[d] Leyden-Jar, Marinus van Meelweg, 5657 EN Eindhoven, the Netherlands
[e] Leiden Institute of Physics – Quantum Matter & Optics, 4, Niels Bohrweg 2, 2333CA Leiden, the Netherlands
[f] TU Eindhoven, EIRES and Department of Applied Physics, the Netherlands

ARTICLE INFO

Keywords:
Thermal plasma
Heat integration
CO_2 conversion
Microwave Plasma
Preheating
CCU

ABSTRACT

We investigated the effects of inlet gas preheating on plasma performance in a vortex-stabilized 915 MHz CO_2 microwave plasma reactor. Spatially resolved spectroscopic measurements of the plasma were employed to understand how preheating affects the temperature profile. Thermographic measurements of the reaction chamber analyzed losses through the wall, offering deeper insights into the thermal changes within the system. The overall conversion performance was evaluated using gas chromatography. We demonstrate that recycling less than 10 % of the input power to preheat CO_2 (T_{inlet} = 700 K) can increase the energy efficiency of CO_2 conversion by up to 1.7 times at conditions near atmospheric pressure (700 mbar), at moderate microwave power (1132 W). The results indicate that preheating affects plasma fluid dynamics, resulting in shifts in plasma contraction and increased spatial temperature profile, or reactive volume, with higher inlet temperatures. This study provides new insights into the potential of integrating heat recycling in plasma reactors for future industrial applications.

1. Introduction

The impacts of anthropogenic climate change are no longer abstract predictions but rather a stark reality affecting communities worldwide. Early reports confirmed by the *Copernicus Climate Change Service* (C3S) of average global temperatures have shown that 2024 is the second year to exceed 1.5 °C above pre-industrial levels [1]. The manifestation of this warming is evident in the unprecedented frequency and intensity of extreme weather events. Escalating climate disasters underscore the immediate need for rapid decarbonization of our energy and industrial sectors. Transitioning to net zero requires not only clean energy but also sustainable carbon-neutral feedstocks to produce the fuels and chemicals that underpin modern society.

The advancement of efficient Carbon Capture and Utilization (CCU) technologies provides a critical pathway towards creating a circular carbon economy. By recycling CO_2 into valuable chemical products and fuels, we can reduce or eliminate greenhouse gas emissions and create sustainable alternatives to fossil-based products. However, the chemical stability of CO_2 presents significant thermodynamic challenges, requiring efficient activation processes that can operate at industrial scales. Microwave (MW) plasma technology has emerged as a leading candidate for CO_2 conversion in a CCU context, demonstrating promising conversion and energy efficiency in laboratory settings due to the high reactivity of plasma [2–6]. Furthermore, the dissociation of feedstock CO_2 using electricity can be achieved using plasma, which matches intermittent renewable energies through on/off switching. This allows

* Correspondence to: E.R. Mercer, Research Group PLASMANT, Department of Chemistry, University of Antwerp, Universiteitsplein 1, 2610 Antwerpen, Belgium.
** Correspondence to: C.F.A.M. van Deursen, Research Group PSFD, Dutch Institute of Fundamental Energy Research, De Zaale 20, 5612AJ Eindhoven, The Netherlands.
E-mail addresses: Elizabeth.Mercer@uantwerpen.be (E.R. Mercer), S.F.A.M.vandeursen@differ.nl (C.F.A.M. van Deursen).
[1] Dual First Authorship
[2] Dual Final Authorship

https://doi.org/10.1016/j.cej.2025.167294
Received 26 March 2025; Received in revised form 17 July 2025; Accepted 14 August 2025
Available online 26 August 2025

for converting these erratic energy sources into precursors for liquid fuels that can be easily stored and used in our existing infrastructure [7]. Moreover, plasma reactors can be integrated into local or regional systems, thereby further reducing CO_2 emissions from transport. While results from the study of MW plasmas are encouraging, the energy efficiency depends critically on operating conditions and reactor design. Achieving industrial viability requires maximizing overall system efficiency.

Recent experimental evidence has revealed that thermal processes play a dominant role in CO_2 dissociation in MW plasmas, with gas temperatures in the plasma core ranging from 3000 K to over 6000 K [2,4,8–11]. This carries significant implications for the design and optimization of MW reactors. The high temperatures observed in the core plasma region, exceeding 1500 K where CO_2 dissociation becomes significant, highlight the importance of thermal dissociation pathways and suggest that careful management of gas temperature and thermal loss mechanisms, from inlet to effluent, are critical for improving overall system performance. Here, it is essential to distinguish between the plasma size and the reactive volume. For thermal processes like CO_2 dissociation, the reactive volume is primarily determined by the temperature distribution rather than electron density [6]. The temperature-defined 'reactive volume' is fundamental to plasma chemistry and represents the region where chemically active species are present in sufficient concentrations, driving reactions. For example, in the work of *Wolf* et al., a plasma diameter of ~2.1 mm was obtained at $p = 500$ mbar, $P =$ 860 W, and a flow rate = 12 slm. In contrast, spectroscopic measurements from the same study reveal elevated temperatures within a reactive area of ~5.0 mm in diameter [9].

In microwave plasmas specifically, the power absorption profile, heat transfer mechanisms, and gas flow dynamics collectively determine the spatial extent of the reactive volume. We characterize this distinction by noting that while the plasma volume is defined by quasi-neutrality and collective behavior of charged particles, the reactive volume encompasses the entire region where plasma-generated species (including excited neutrals, radicals, and metastable species) participate in reactions that provide products of interest. Since it is well established that reactor performance is largely governed by high-temperature thermal chemistry [2,6,7,10,12–14], strategic heat recovery could significantly enhance overall system efficiency. These insights also suggest that preheating the inlet gas could enhance reaction kinetics while reducing the overall energy requirement for achieving dissociation temperatures.

The concept of heat recovery in plasma systems has historical precedents. The Schönherr process for nitrogen fixation, developed in the early 1900s, demonstrated preheating inlet gas using waste heat [15,16]. Similarly, the Birkeland-Eyde process utilized heat exchangers to improve the efficiency of their atmospheric nitrogen fixation system [17]. The Hüls process for acetylene production from hydrocarbons provides another historical example of successful heat management in plasma processes [18,19]. These industrial-scale applications demonstrate that careful management of thermal energy is crucial for process economics in plasma-based chemical conversion. Modern industrial applications of plasma technology could benefit from similar heat recovery strategies. Recent studies have shown that gas-to-gas heat exchangers can significantly improve energy efficiencies in chemical processing [20]. In MW plasma systems specifically, the high temperatures achieved in plasma (>> 3000 K) represent a substantial source of thermal energy that could be recovered. While MW plasma technology for CO_2 conversion has been extensively studied, research specifically investigating preheating effects remains limited and has primarily been conducted in other plasma systems. To address the lack of systematic research into the effects of preheating in plasma reactors, especially in MW plasmas, this paper aims to study the effects on contraction dynamics, thermal profiles, power loss distributions, as well as conversion and energy efficiency to understand the underlying effects of preheating the input gas.

Shenoy et al. demonstrated the benefits of preheating in a non-thermal gliding arc plasma for natural gas reforming to syngas, showing that preheating up to 800 K could reduce specific energy requirements by enhancing conversion [21]. *Cho* et al. developed a 'double helix' gas injection system that passively preheats the inlet gas by routing it around the discharge tube before entering the plasma, demonstrating improved CO_2 conversion and energy efficiency compared to conventional MW plasma generators; however, the authors did not report inlet temperatures, so a deeper understanding of the benefits is limited [22]. *Jo* et al. investigated preheating effects up to 400 K on methane oxidation in gliding arc plasma reforming, showing that identical efficiencies could be achieved with lower total input power by applying some of the power to preheating [23]. In plasma-based reactions, preheating the inlet gas stream has the potential to influence various aspects of plasma dynamics significantly, such as altering the internal energy distribution, which can affect reaction volume, radiative losses, particle transport, and energy exchange rates.

To the authors' knowledge, systematic studies investigating preheating effects, particularly at 915 MHz, have not been reported for CO_2 MW plasmas. Given that preheating could influence plasma behavior by modifying gas density, flow dynamics, and plasma contraction mechanisms, understanding these effects represents a fundamental knowledge gap for optimizing MW plasma reactor performance. The aim of this work is to investigate the effects of preheating inlet CO_2 gas in a plasma reactor in order to gain insight for future industrial systems by understanding the potential benefits of implementing waste heat utilization. More specifically, we will study how preheating modifies plasma behavior and contraction dynamics in a vortex-stabilized 915 MHz CO_2 plasma reactor by exploring underlying mechanisms, as deeper understanding of these effects is an important step for optimizing total plasma reactor efficiency in an industrial setting. Therefore, the main aim of this study was not to obtain the highest performance, but to gain more insight in the underlying mechanisms and how they can contribute to better performance. The influence of preheating on plasma characteristics is examined with respect to its effects on the reactive volume through an investigation of the spatial temperature distribution. A key consideration is the impact of preheating on thermal management and heat losses at the reactor walls, which could have significant implications for the system's energy efficiency. Additionally, this study evaluated the role of preheating in enhancing CO_2 conversion and energy efficiency across various pressure regimes and operating conditions. Finally, the potential for preheating to partially offset MW power requirements while maintaining plasma performance is explored, offering insights into optimizing energy input for sustainable plasma processes.

2. Experimental setup

The experimental setup consists of a vortex-stabilized waveguided MW plasma reactor (*Fig. 1**A***) with a GaN solid-state MW source with a rated efficiency of ~42 % (Wattsine, WSPS-915-5000) that emits an adjustable Continuous Wave (CW) power up to 5 kW at a set frequency of 915 MHz. The MW power is transmitted through a WR975 rectangular waveguide in TE_{10} mode, forming a standing wave. The MW generator is protected by an isolator (*Fig. 1**B***), which prevents any reflected power from returning upstream. Matching components consist of an automatic stub tuner (HOMER S-TEAM STHT V2.3) (*Fig. 1**C***) set between the generator (MW source) and the resonance chamber (*Fig. 1**D***) ensuring a high coupling efficiency by matching the impedance, so that reflected power remains below 1 % during experiments. The autotuner also measures the forward and reflected power and frequency applied to the CO_2 gas flow passing perpendicularly through the resonance chamber in a 27 mm inner diameter Quartz Tube (*QT*). A *QT* containing the gas flow traverses the shorted waveguide (*Fig. 1**D***). The gas was tangentially injected from the preheating section (*Fig. 1**E***) into the reactor volume by two quartz tubes to create the stabilizing vortex flow. To avoid leak sensitive material transitions, the preheating section and the reactor

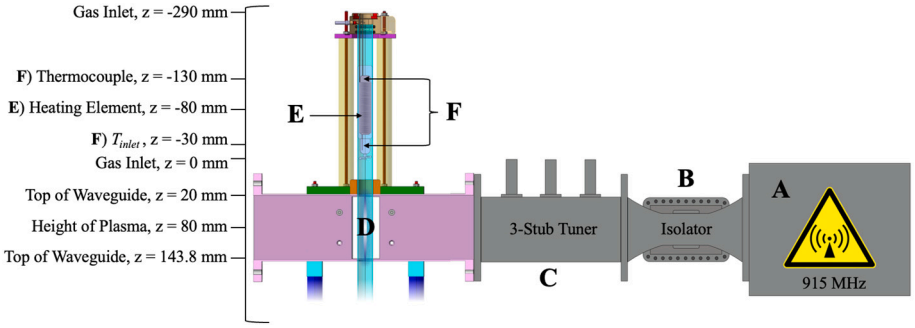

Fig. 1. Schematic overview of the experimental setup. From right to left, (**A**) the 915 MHz solid-state MW source (Wattsine, WSPS-915-5000) in a WR975 waveguide, (**B**) the isolator, (**C**) the automatic stub tuner (HOMER S-TEAM STHT V2.3), and (**D**) the 27 mm inner diameter QT viewed though the cut-off tube. The (**E**) heating element and (**F**) thermocouples were positioned above the reaction chamber.

section were integrated in a single quartz tube and separated by a quartz disc. The reactor has two diagnostic viewing ports perpendicular to the waveguide formed by open metal rectangular tubes (length 30 cm) in cut-off to prevent MW leakage.

The preheating system consisted of a custom-designed heating element (*Fig. 1**E***) positioned 200 mm above the resonance chamber (*Fig. 1**D***) of the waveguide. The heating element was constructed from 1 mm diameter Kanthal A1 (FeCrAl) wire with a measured total resistance of 3.5 Ω. The wire was insulated with alumina beads (to prevent shorting), supported by an alumina tube, and secured in place using high-temperature ceramic adhesive. Temperature monitoring of the inlet gas was accomplished using K-type thermocouples (TC Direct) (*Fig. 1**F***). One thermocouple measured the heater temperature directly, while a second thermocouple was positioned immediately upstream of the tangential gas injection to measure the gas inlet temperature (T_{inlet}). This T_{inlet} measurement provided an accurate representation of the gas temperature immediately before entering the resonance chamber (*Fig. 1*D). To enhance thermal efficiency and minimize heat loss, the *QT*

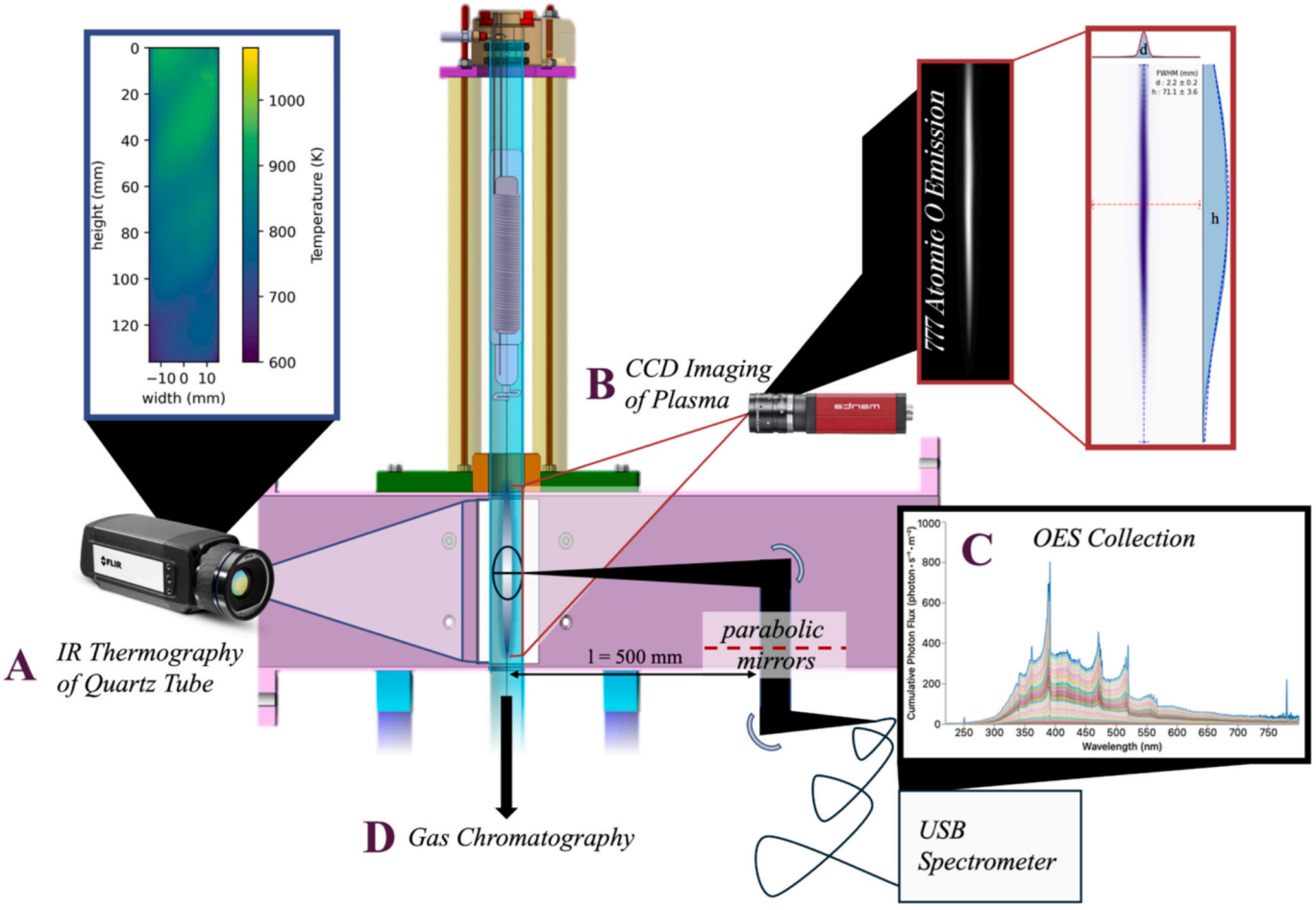

Fig. 2. From left to right: (**A**) Infrared thermographic imaging was taken of the QT to calculate the thermal losses through the wall, (**B**) plasma imaging of the 777 nm atomic oxygen emission was collected using a CCD camera, treated to derive the plasma diameter (d) and the height (h) based on the intensity profile, (**C**) a radially resolved optical emission profile was collected using stages consisting of parabolic mirrors and a fiber attachment with a focal point calculated to be 0.5 mm. The collected spectra were pretreated and then fit the C_2 Swan bands for the central temperature profiles using MassiveOES as well as with the flame band model for the periphery temperatures. Gas chromatography (**D**) was utilized to measure the effluent gas stream.

surrounding the heating element was insulated with aluminum oxide wool. This insulation significantly improved heating efficiency by reducing radiative and convective heat losses through the quartz walls.

2.1. Diagnostics and performance metrics

A comprehensive overview of the experimental diagnostics setup, including thermographic measurements and collection optics is presented in Fig. 2. The diagram illustrates the spatial arrangement and configuration of all measurement instruments used to characterize system performance.

The total dissipated power lost through the *QT* wall was measured using an InfraRed (IR) thermography camera (FLIR A655sc) equipped with a 41.3 mm lens and an open calibrated filter with a spectral range of 7.5–14 μm (Fig. 2***A***). The collected data from IR measurements aids in understanding the power loss to the environment through the *QT* at the height of the plasma and its impact on system performance. The radiated power was calculated using Stefan-Boltzmann's Law. The reported radiated power and temperature loss through the wall were calculated using the method reported in *van Deursen* et al. [5]. The convection loss through the wall were calculated using the method outlined in *Supplementary Information (SI), Section 1*. As shown in Fig. 2***B***, the optical plasma emission was captured using a CCD camera (Allied Vision Manta G-146B) equipped with a 780 nm narrow bandpass interference filter to isolate oxygen lines at 777 nm and a neutral density filter to prevent overexposure of the CCD. The emission intensity was utilized to derive the shape, size, and volume of the plasma profile. Reported plasma height and diameter were derived using the method described by *Wolf* et al. [24].

An optical stage was used to scan the *QT* (the reaction chamber) using optical emission spectroscopy (OES) at the height of the plasma through the viewing ports (Fig. 2***C***) using an Ocean Insight mini spectrometer (FLAME-S) with an optical resolution 0.9 nm equipped with a custom 20 cm, 400 μm high-OH core fiber (Thorlabs FG400AEA). The radial temperature profile is derived using two unique spectral characteristics commonly found in contracted CO_2 MW plasmas. Additional details optics and preprocessing of the spectral data can be referenced in the *SI, Section 2*. The C_2 ($d^3\Pi_g - a^3\Pi_u$) Swan band system can be utilized to derive the rotational and vibrational temperatures [8]. We can, therefore, exploit this spectral feature to derive the core plasma temperature profile, under the assumption that the rotational temperature is equal to the gas temperature. Details of the data processing and uncertainty of the MassiveOES fits can also be found in *SI, Section 2*. Flame band emission spectroscopy was utilized as a secondary temperature diagnostic to capture the periphery temperatures surrounding the core plasma region. Flame band spectroscopy measures the emission intensity from the radiative transition of excited CO_2 to ground-state CO_2 after recombination of CO and O [25]. Details of the data processing, fitting routine, error analysis, and uncertainty of the flame band fitting can also be found in *SI, Section 2*.

We utilize Gas Chromatography (GC) (*G.A.S. Compact GC 4.0*) to measure the composition of the post-plasma effluent mixture (Fig. 2***C***). From this, the conversion and energy efficiency were calculated using the methods outlined by *Wanten* et al. [26]. *SI, Section 3* outlines further details on analytical techniques and performance calculations. The methods used to calculate the power to heat CO_2 (P_{CO_2}) can be referenced in *SI, Section 4*.

2.2. Experimental outline

To comprehensively assess the preheating effects on CO_2 conversion in a MW plasma, two experimental series were investigated:

1) ***Constant MW Power Measurements***: In this series of experiments, the MW power (P_{MW}) was held constant, while the inlet mass flow rate of CO_2 was preheated to set temperatures. This approach simulates scenarios where heat recycling could be leveraged to enhance conversion, while providing insight into overall changes in performance. Since the P_{CO_2} used for preheating is assumed to originate from waste heat recovery, it is excluded from the energy efficiency calculation, which normally only accounts for the MW power coupled to the chemistry. By maintaining constant P_{MW}, this experiment is designed to isolate the thermal enhancement effects on plasma performance.
2) ***Constant Total Power Measurements***: The total input power to the system ($P_{total} = P_{MW} + P_{CO_2}$) was held constant, isolating the role of preheating in reducing the required MW power on conversion rate. This set of experiments directly evaluates whether preheating allows for a proportional reduction in P_{MW}, while maintaining or improving dissociation efficiency. The assumption remains that P_{CO_2} originates from heat recovery and is therefore decoupled from the energy efficiency calculation, ensuring that any observed gains in performance reflect the redistribution of power rather than an increase in total energy input.

The benchmark condition with a $T_{inlet} = 300$ K serves as the baseline reference and is represented in green throughout the text.

3. Results and discussion

The results presented in this section were investigated at varying power levels and T_{inlet} with a mass flow rate (ϕ_{CO_2}) of 10 normal liters per minute (ln/min - STP IUPAC, 0 °C, 1 bar) [26]. First, we discuss the reactor performance, analyzed in terms of CO_2 conversion (χ) and energy efficiency (η). Next, we explore the effects of preheating on the plasma characteristics, focusing on changes to the reaction volume ($T_{gas} > 1500$ K, where dissociation of CO_2 to CO becomes significant) and plasma size (diameter and length as determined by the FWHM of the 777 nm atomic oxygen emission intensity), as well as the effects on radiated power through the reactor wall as measured by IR thermography. The performance metrics are correlated with the radial gas temperature profiles at the plasma height, and the heat flux through the reaction chamber wall, where we analyze the overall impact of gas preheating on conversion, energy efficiency, and plasma dynamics.

3.1. Preheating effects on conversion and energy efficiency

Fig. 3 presents a comparative look at conversion and energy efficiency between constant P_{total} and P_{MW}. All conditions are represented with a $\phi_{CO_2} = 10$ ln/min, and varying $T_{inlet} = 300$ (green), 500 (yellow), and 700 K (orange), which correspond to $P_{CO_2} = 0$, 62, and 132 W, respectively. The results for constant $P_{total} = 1132$ W are shown on the lefthand side (Fig. 3*A* and Fig. 3*B*), while constant $P_{MW} = 1000$ W is on the righthand side (Fig. 3*D*). A visualization of the plasma imaging defined by the 777 nm atomic oxygen emission is shown for $p = 150$ mbar and different T_{inlet} (Fig. 3*C*).

Fig. 3*A* and Fig. 3*B* reveal that at near-atmospheric pressure ($p =$ 700–900 mbar), preheating provides modest but measurable benefits to the conversion and energy efficiency. When P_{total} is kept constant, conversion increases by ~1.2 at 700 mbar for $T_{inlet} = 700$ K and ~ 1.1 at 900 mbar for $T_{inlet} = 500$ K compared to baseline conditions. The reader should note that in literature typical conversion in atmospheric CO_2 MW plasmas is reported around 10 % [2,4,8–11]; however, as this study represents a first approach to preheating, the reactor configuration was not optimized by downstream quenching (to avoid back-reactions), and thus benchmark conversion is lower (~5 %). This is likely a result of the specialized quartz injection housing and non-optimized flow dynamics in the system. The data for $T_{inlet} = 700$ K at $p = 900$ mbar is unavailable due to plasma instability. On the other hand, at low pressure ($p = 200$ mbar), preheating reduces conversion at higher T_{inlet}, with values dropping from 23.92 ± 0.09 % at 300 K to 18.26 ± 0.07 % at 700 K.

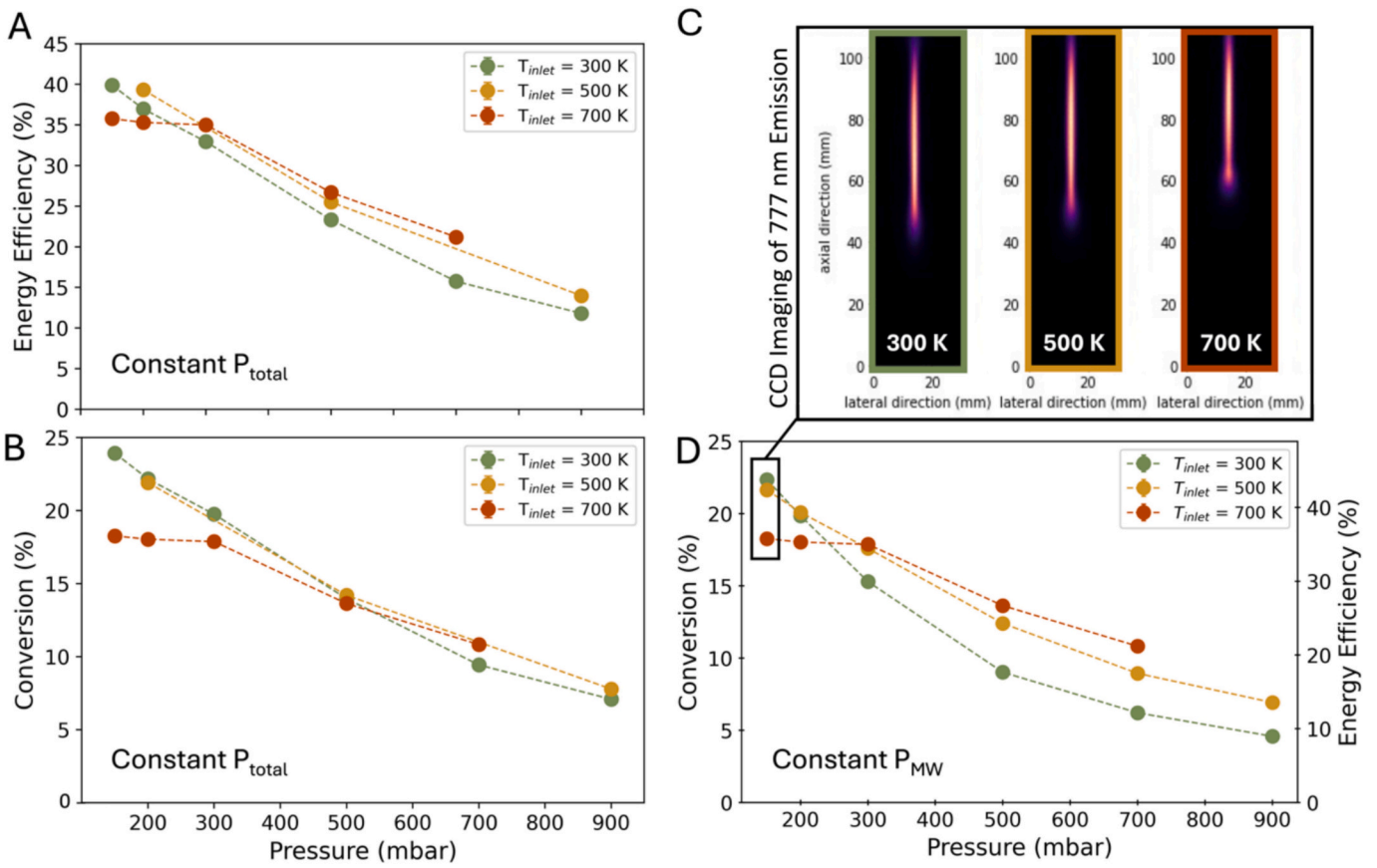

Fig. 3. Conversion and energy efficiency for T_{inlet} = 300 K (green), 500 K (yellow), 700 K (dark orange) as a function of pressure, at constant P_{total} = 1132 W (A, B) or constant P_{MW} = 1000 W (D). Panel C represents the CCD images of the plasma emission profile for the atomic oxygen (777 nm) for the indicated data points at p = 150 mbar. All conditions were taken with ϕ_{CO_2} = 10 ln/min. Error bars are given but fall under the data markers in all cases.

Fig. 3D shows larger improvements to the conversion and energy efficiency at constant P_{MW} = 1000 W, which is logical, because the power used to preheat the inlet CO_2 is 'freely' added to the system, enhancing conversion, and it is not used to calculate energy efficiency, which thus rises to the same extent as conversion (see *SI, Section 4*, for additional information on the calculations used). However, at low pressure (p < 200 mbar), elevated inlet temperatures (500 K and 700 K) negatively impact energy efficiency and conversion. For example, at 150 mbar, increasing T_{inlet} from 300 K to 700 K reduces conversion from 22.35 ± 0.09 % to 18.26 ± 0.09 %. This is likely a consequence of the plasma contraction state.

Indeed, it is well documented that CO_2 MW plasmas exhibit distinct discharge modes characterized into three categories, which are broadly determined by power, pressure, and gas flow rate [9,11,13]. At low pressure (< 100 mbar) or power density, the plasma often remains in homogeneous or L-mode, as characterized by uniform temperature, as well as relatively low power density profiles [9]. As pressure increases, the hybrid mode arises (typically between 100 and 200 mbar), balancing partial contraction with sufficient homogeneity to maintain high energy efficiency and mixing [9]. We observe that the benchmark condition for 150 mbar shows hybrid characteristics, where the center region of the filament is contracted but grows outward towards the tip of the column (*Fig. 3C*). With increasing T_{inlet} these characteristics become more pronounced, accompanied by a notable decrease in the plasma length (axial direction), as defined by the FWHM of the 777 nm atomic oxygen emission profile for all conditions presented (see again *Fig. 3C*). The decrease in plasma length (along with a drop in radial temperature profile, i.e., reactive area) may explain the observed decline in performance at 150 mbar (*Fig. 3D*), due to the reduced reactive volume.

Above ~200 mbar, steep radial gradients arise, leading to a contracted mode (H-mode). These transitions are driven by thermal-chemical instability [9,11,27,28], where localized heating boosts ionization rates, creating dense filaments with elevated temperatures and enhanced MW absorption [27]. We see the trend of conversion and energy efficiency upon preheating reverses as the pressure increases and the hybrid mode shifts to fully contracted H-mode, resulting in preheating enhancing both conversion and energy efficiency. Notably in *Fig. 3D*, for P_{MW} = 1000 W at near-atmospheric pressure (900 mbar), T_{inlet} = 500 K achieves a 1.5-time relative increase in conversion compared to 300 K (6.92 ± 0.02 % vs. 4.58 ± 0.01 %, respectively). A similar pattern is observed at 700 mbar, where T_{inlet} = 700 K demonstrates a 1.7 time improvement over the baseline of 300 K (10.82 ± 0.04 % vs. 6.21 ± 0.02 %, respectively).

Several mechanisms govern contraction. Electron collisions (particularly in the plasma core) can increase ionization rates, while radial temperature gradients modify the reduced electric field and reduce charged-particle losses [29]. This positive feedback leads to narrow, high-power density regions with significant temperature elevation; however, it can limit the overall reactive volume, as contracted (H-mode) plasmas will exhibit a reduced interface between the reactive volume and the bulk gas of the reaction chamber. Consequently, the hybrid regime often emerges as the optimal mode for CO_2 conversion, balancing localized heating with adequate mixing and quenching. However, this regime requires vacuum pumping, which uses additional power from plug to product [30].

Despite the change in power distribution (whether constant P_{total} or P_{MW}), we observe that preheating the inlet gas has a marked improvement on conversion and energy efficiency at near-atmospheric pressure, while at low pressure (≤ 200 mbar) there is a decline in performance. Our results suggest that partial substitution of MW power with direct gas

heating can improve conversion and energy efficiency at higher pressures, which is especially important when considering that operating at higher pressures also reduces power consumption needed for vacuum pumping. The modest improvements shown with $P_{total} = 1132$ W at near-atmospheric pressure likely stem from compounding mechanisms, such as the potential for increased post-plasma recombination or reduced gas residence time within the reactive volume. Therefore, a deeper understanding of the underlying mechanisms is crucial for optimization. These effects will be further investigated in the following sections.

Having established the baseline behavior for constant P_{total} and P_{MW}, we will now examine how these preheating effects manifest at slightly higher power. Increasing the input power while maintaining the same mass flow rate provides insight into whether the observed preheating benefits scale with specific energy input. Furthermore, we captured additional T_{inlet} conditions to broaden the parameter space and our understanding of the effects of preheating. *Fig. 4* presents experimental results obtained for $P_{total} = 1500$ W, $\phi_{CO_2} = 10$ ln/min, $T_{inlet} = 300$ K (green), 500 K (yellow), 700 K (orange), and 850 K (brown) at varying pressure.

Fig. 4A and *Fig. 4B* reveal several important trends in how T_{inlet} affects CO_2 conversion and energy efficiency across different pressures. The most striking observation is that $T_{inlet} > 300$ K and within the contracted plasma regime ($p > 200$ mbar) consistently yields better energy efficiency and conversion (*Fig. 4A,B*). An investigation into the effects of increasing the input power and mass flow rate can be reviewed in *SI, Section 5*; however, the reader can note that the conclusions remain consistent with the main findings reported in this section. At $p = 200$ mbar, conversion peaks around 25 % ($T_{inlet} = 300$ K, 500 K, 700 K, and 850 K give 25.45 ± 0.11 %, 26.34 ± 0.11 %, 25.50 ± 0.11 %, 24.49 ± 0.10 %, respectively), showing relatively small variation between different inlet temperatures. As pressure increases, the performance advantage of preheated conditions becomes more pronounced. As also shown in *Fig. 4C*, the divergence between the baseline and preheated conditions (500–850 K) grows larger at higher pressures, with preheated conditions maintaining significantly better conversion up to 900 mbar ($T_{inlet} = 300$ K, 500 K, 700 K, and 850 K give 5.34 ± 0.02 %, 8.56 ± 0.03 %, 8.52 ± 0.03 %, 6.84 ± 0.02 %, respectively). Thus, preheating extends the pressure range for efficient conversion, although the data shows the highest inlet temperature, $T_{inlet} = 850$ K, does not yield the highest conversion (*Fig. 4C*), indicating an optimal ratio between P_{CO_2} and P_{total}.

3.2. Preheating effects on the reactive area

Radial scans at the height of the plasma were performed using OES to

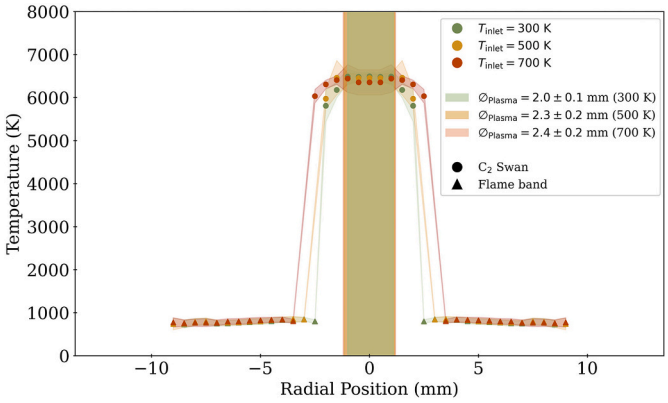

Fig. 5. Radial temperature profiles for $P_{MW} = 1000$ W, $\phi_{CO_2} = 10$ ln/min, $T_{inlet} = 300$ K (green), 500 K (yellow), 700 K (dark orange) for $p = 700$ mbar. The center-shaded region represents the plasma diameter, determined by the FWHM of the emission intensity of the 777 nm atomic oxygen line captured by CCD imaging. The temperatures derived from the C_2 Swan band emission are represented as circles and from the flame band as triangles.

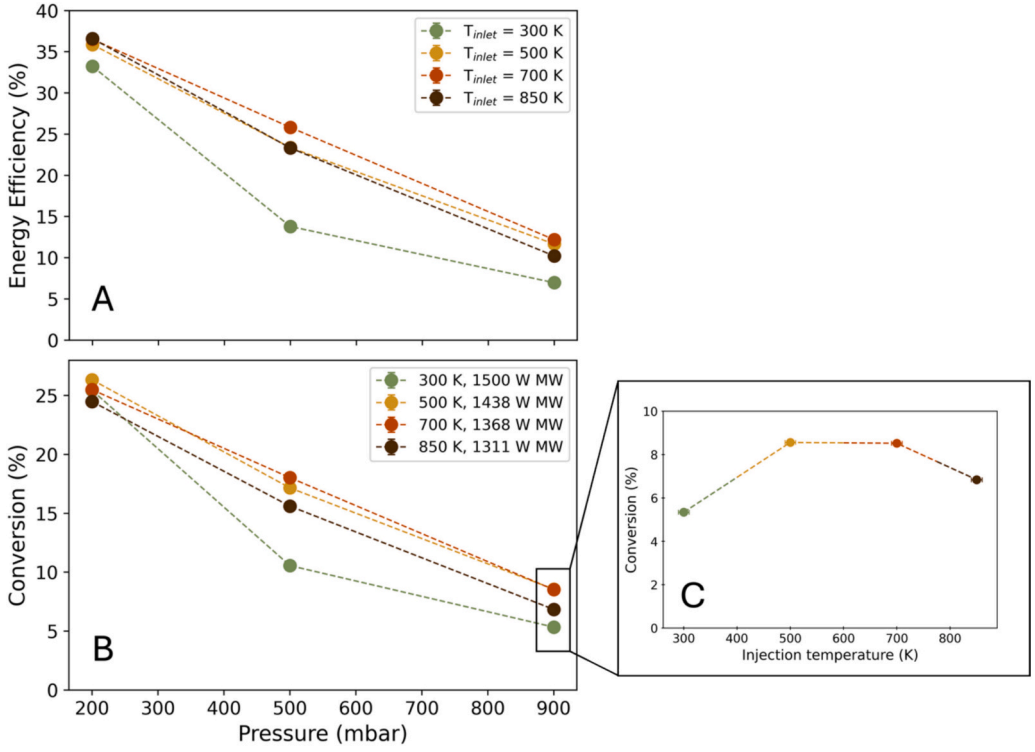

Fig. 4. (A and B) Energy efficiency and conversion as a function of pressure, for $P_{total} = 1500$ W, $\phi_{CO_2} = 10$ nlm, $T_{inlet} = 300$ K (green), 500 K (yellow), 700 K (orange) and 850 K (brown). (C) shows the conversion for $p = 900$ mbar as a function of T_{inlet}, to highlight the decrease in conversion observed at $T_{inlet} = 850$ K. The total power added to the system was kept constant across all measurements. Error bars are given but fall under the data markers in all cases.

explore the connection between preheating and plasma behavior. *Fig. 5* shows the radial temperature profiles at P_{MW} = 1000 W, ϕ_{CO_2} = 10 ln/min, and p = 700 mbar, for three T_{inlet} conditions. The pressure series of 700 mbar was chosen for a comparative view, given that plasma instability did not allow for 900 mbar measurements at T_{inlet} = 700 K p = 900 mbar. For additional radial temperature profiles, please see *SI, Section 5*. Radially resolved C_2 Swan band emissions (shown as the circle data points) provided plasma core temperatures (T = ~ 6000–7000 K), while flame band emissions (shown as triangular data points) characterized peripheral temperatures (T < 1500 K).

In *Fig. 5*, the shaded regions within the center of the radial temperature profile represent the plasma diameter determined by the 777 nm atomic oxygen emission captured by CCD imaging. Here, we must make a distinction between the plasma diameter and the elevated temperature region, which extends out of the cylindrical plasma volume, and which we denote as the 'reactive volume', where T_{gas} >> 1500 K, i.e., the threshold temperature for CO_2 dissociation [14]. In *Fig. 5*, we observe that the plasma diameter increases with increasing T_{inlet}, being 2.0 ± 0.1, 2.3 ± 0.2, and 2.4 ± 0.2 mm, at 300, 500, and 700 K, respectively, and we also note a clear difference in the overall reactive area (represented by the last data point from the C_2 Swan band emission) between different T_{inlet}, where the spatial temperature distribution becomes broader with increasing T_{inlet}. This is most easily observed in the transparent interpolated line between the C_2 swan-derived temperatures (circles) and the flame band-derived temperatures (triangles); however, it should be stressed that these connections are for visualization purposes only.

These results further indicate that preheating affects plasma contraction dynamics, likely due to increased volumetric flow rates driven by higher T_{inlet}. Since elevated T_{inlet} reduces gas density (n), there will be a proportional increase in the volumetric flow rate ($Q = \phi_{mass}/n$) at a constant mass flow rate (ϕ_{mass}). Consequently, the average gas velocity rises at a fixed cross-sectional area, likely shortening the residence time (τ) of reactants in the plasma, potentially affecting conversion. The broadening of the temperature profile shown in *Fig. 5* suggests enhanced convective cooling, as well as (turbulent) mixing due to high surface to volume ratio, such that heat is removed more efficiently from the reactive volume, reducing the local temperature gradient that drives contraction. Further evidence of this can be explored in *SI, Section 5*. Two critical observations remain consistent across all conditions. First, the core temperature remains consistent at ~6000 K regardless of T_{inlet}, indicating that electron-neutral coupling in the plasma core remains unaffected by preheating. Second, the peripheral temperatures derived from flame band emission measurements remain below 1500 K for all T_{inlet}. This temperature is sufficiently low to effectively quench products radially diffusing from the reactive volume [14]. These findings suggest that while preheating notably influences the spatial distribution of the plasma and reactive volume, it does not fundamentally alter the core plasma properties or peripheral quenching conditions.

A clear correlation emerges between the broadened temperature profile observed in *Fig. 5* and the enhanced conversion under these conditions. As discussed in *Fig. 5*, in all cases, the reactive area is larger than the dimensions of the plasma filament determined by the 777 nm atomic oxygen emission. For example, at T_{inlet} = 700 K, the plasma diameter was found to be 2.4 mm versus 5.0 mm as derived from the C_2 swan band temperature profile. To explore this further, we consider the available temperature data, where T >> 3000 K and CO_2 dissociation becomes significant, as a slice of the reactive volume. As a first estimate, we utilize the interpolated radial position of the cross-section where T = 3000 K (the shaded line connecting the C_2 Swan band and the flame band temperatures) to approximate the reactive area at the height of the plasma, as shown in *Fig. 6*.

In *Fig. 6*, we observe that the estimated reactive area is ~30, 20, 17 mm^2 for T_{inlet} = 700, 500, and 300 K, respectively. As an example, the reactive area between T_{inlet} = 700 and 300 K accounts for a relative increase of ~1.8, whereas the values between T_{inlet} = 500 and 300 K, account for an increase of ~1.2 times. We would like stress that this is a first estimate for these values; however, we observe that the trend in the relative increase of the reactive area correlates to the increased conversion observed in *Fig. 3D*.

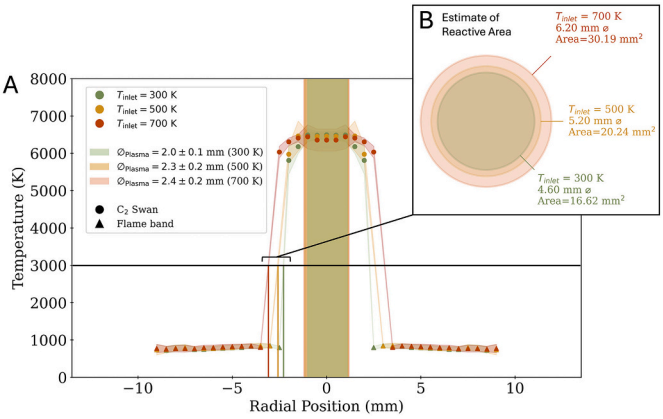

Fig. 6. Reactive area (T >> 1500 K) for P_{MW} = 1000 W, ϕ_{CO_2} = 10 ln/min, T_{inlet} = 300 K (green), 500 K (yellow) and 700 K (dark orange), for p = 700 mbar, where (A) is the C_2 swan band and flame band derived temperature profile (cf. Fig. 5). The interpolated radial position at T = 3000 K is taken as an approximation for a slice of the reactive volume, and is used to calculate the reactive area, visualized in (B).

As shown in *Fig. 7*, the expansion of the reactive area with T_{inlet} = 700 K and 500 K trends correlate with the increased conversion at these conditions, where an improvement of approximately 1.7 and 1.4-fold, respectively, over baseline conditions (cf. also *Fig. 3D*) was reported at 700 mbar. Preheating influences both volumetric flow rate and mass transport. Considering an equal mass flow rate, preheating the inlet gas will increase the volumetric flow rate, thereby enhancing convective cooling and allowing for more efficient heat removal from the reactive volume. This would decrease the local temperature gradient that induces plasma contraction, causingthe heat to distribute over a larger area. These findings support the hypothesis that preheating the inlet gas leads to a broader reactive volume, which likely contributes to the improved conversion observed at these conditions. The expanded interface between the reactive volume and the cooler periphery region could enhance mixing between the reactive molecules and the bulk gas, leading to additional products being carried out of the reactive volume.

3.3. Preheating effects on power loss through the wall

The thermal behavior of the reactor walls during plasma operation

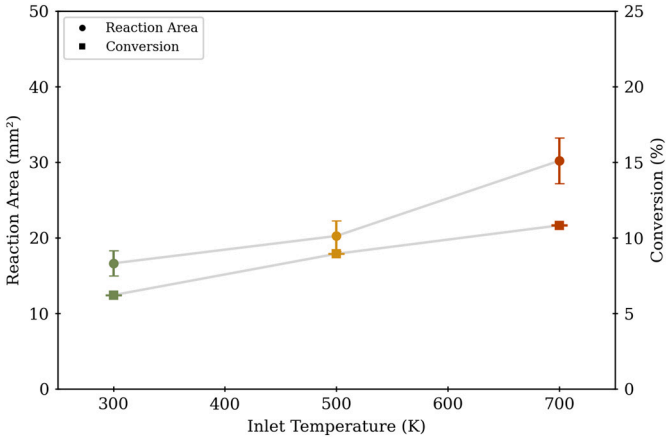

Fig. 7. Estimated reactive area and conversion plotted as a function of T_{inlet} (K). A clear correlation emerges between the reactive area and conversion.

provides additional insight into how preheating affects overall system performance and energy distribution. *Fig. 8* shows thermal imaging of the *QT* inside the waveguide at different inlet temperatures, for P_{total} = 1500 W, ϕ_{CO_2} = 10 ln/min, p = 900 mbar and T_{inlet} = 300, 500, 700, and 850 K, corresponding to preheating power (P_{CO_2}) = 0, 62, 132, and 189 W, respectively.

The results presented in *Fig. 8* reveal two key phenomena: 1) a downward shift in the position of the peak wall temperature with increasing T_{inlet} that falls inside the vortex flow lines, demonstrating the heating and cooling on the surface *QT* and 2) increased radiative losses with increasing T_{inlet}, as calculated by Stefan-Boltzmann's law. These observations can be explained through several mechanisms. First, the preheated input flow is the likely culprit for the slight increase in the average temperature observed in the top half of the reaction chamber (*Fig. 8B*). For example, at T_{inlet} = 300 K, the T_{avg} is 885 K vs at T_{inlet} = 850 K, the T_{avg} increases to 951 K. However, the downward migration of the peak temperature zone observed (*Fig. 8C*) cannot be attributed solely to the preheated inlet gas flow, which would primarily affect the upper region of the tube. Furthermore, in *Fig. 5*, we observed that the periphery temperatures derived from the flame band emission remain relatively consistent regardless of T_{inlet}, which is further demonstrated by additional data provided in *SI, Section 5*. Therefore, we consider this increased temperature on the surface of the *QT* is likely caused by an increase in exothermic recombination reactions, consistent with previous observations by *Wolf* et al. [14] and *van Deursen* et al. [5].

It is also worth noting that the helical vortex flow structure remains clearly visible in all IR images throughout the entire *QT*, from top to bottom. The darker spiral bands indicate where the cooler input gas flows along the *QT* walls, demonstrating that the vortex structure maintains its integrity as it passes around the reactive volume. This visualization of the flow lines provides important evidence supporting our analysis of the temperature distribution patterns observed in *Fig. 8B* and *Fig. 8C*, helping to explain the downward migration of peak temperatures with increasing T_{inlet}, as the helical flow patterns appear to influence heat transfer and reaction zone positioning throughout the reactor. This hypothesis is further substantiated when we consider the relationship between the total dissipated power (radiative + convective) with T_{inlet}, as well as between radiated power for the top half and bottom half of the *QT* with T_{inlet}, as shown in *Fig. 9(A,B)*.

Fig. 9A shows the total dissipated power (W) from the *QT* as a function of T_{inlet} from 300 K to 850 K, while *Fig. 9B* shows the radiative losses for the top and the bottom half (see legend), as split in *Fig. 8B*. Both curves show an overall increasing trend in radiated power as T_{inlet} increases, but the rise is more pronounced for the bottom half. These findings suggest that preheating primarily affects upstream flow dynamics, which then influence the reactive cross section (*Fig. 5*), and thus, the reactive volume interface (*Fig. 6*). This is further validated by the increase in total losses being greater than the power added through preheating, suggesting that this increase is due to changes in flow dynamics and/or an increase in recombination. The radiated heat pattern (*Fig. 8*) also provides evidence for significant atomic oxygen recombination:

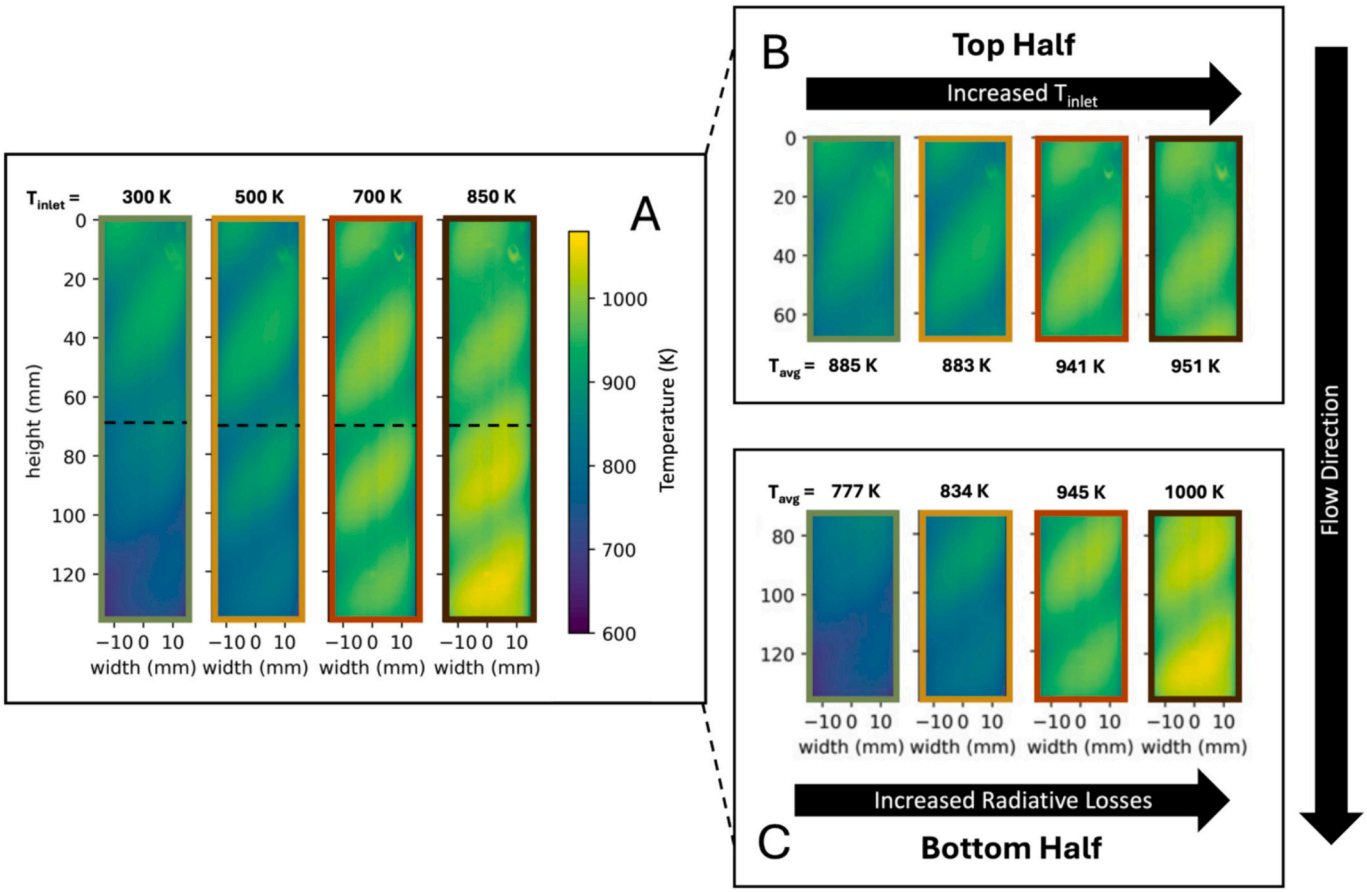

Fig. 8. (A) Thermal images of the *QT* inside the waveguide at different inlet temperatures, for P_{total} = 1500 W, ϕ_{CO_2} = 10 ln/min, p = 900 mbar, and T_{inlet} = 300, 500, 700, and 850 K, where P_{CO_2} = 0, 62, 132, 189 W, respectively. The images show a downward shift in the position of peak wall temperature with increasing T_{inlet}, and they also illustrate the heating and cooling caused by the flow lines of the helical vortex, visible in the IR images. A pixel-by-pixel analysis (right) provides an average temperature (T_{avg}) for the top (B) and bottom half (C) of the thermographic image, showing the correlation with increasing T_{inlet} (top half, B) and increased exothermic recombination (bottom half, C). For reference, the reported OES measurements were taken in the middle of the waveguide, where the dashed line is indicated.

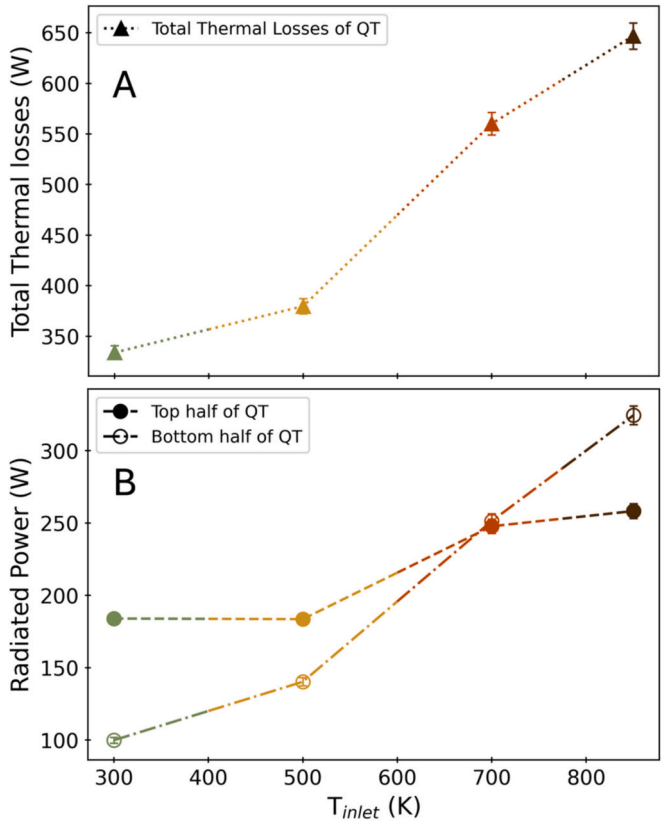

Fig. 9. (A) Total dissipated power (radiative + conductive) as a function of T_{inlet}, showing that the total losses increase with increasing T_{inlet}, (B) Radiated power (calculated using Stefan-Boltzmann's law from the calculated pixel-by-pixel T_{avg}, indicated in Fig. 8) for both top and bottom half, as a function of T_{inlet}. The increase of the radiative power for the top half and the bottom half of the *QT* reaches a crossover point at $T_{inlet} = 700$ K.

$$O + O + M \rightarrow O_2 + M, \Delta H = -5.18\ eV \quad \text{(R.1)}$$

or atomic oxygen recombination with CO, the origin of chemiluminescent flame band emission, simplified as:

$$CO + O + M \rightarrow CO_2 + h\nu + M, \Delta H = -5.53\ eV \quad \text{(R.2)}$$

between the plasma and downstream region, as atomic oxygen, produced at the same rate as CO, would generate substantial heat during recombination [4,14,31]. Furthermore, these reactions will increase with pressure due to the third body collisional factor. Therefore, any gains in conversion due to increases in the reactive volume are likely lost due to downstream recombination. *Vertongen* et al. showed that although atomic oxygen plays a crucial role in efficient CO_2 dissociation, the presence of atomic oxygen in the effluent also enhances the rate of recombination, decreasing overall conversion [32].

In summary, the observed downward shift in temperature distribution with increasing T_{inlet} confirms that complex interactions exist between flow patterns and heat transfer. These findings demonstrate that preheating effects on plasma behavior are highly pressure dependent. Moreover, the temperature profiles reveal that peripheral temperatures remain below 1500 K across all T_{inlet} conditions, maintaining effective quenching capability for the back reaction of CO + O. However, thermal imaging shows that preheating increases radiative losses through the reactor walls and shifts the peak temperature zone downward. This redistribution of thermal energy suggests modified flow patterns and potentially accelerated recombination processes in the downstream region, particularly evident in the enhanced heat release patterns observed with higher inlet temperatures. The preservation of the peripheral temperature profile, and its relation to effective quenching, despite increased T_{inlet}, is particularly noteworthy, as it indicates that preheating primarily influences upstream flow dynamics and reactive volume distribution, without compromising conversion to CO. However, the increased wall losses and evidence of enhanced recombination suggest that optimizing thermal management in the downstream region becomes increasingly critical at higher T_{inlet}.

4. Conclusions and outlook

Our investigation of inlet gas preheating in a 915 MHz CO_2 MW plasma reveals distinct effects on the spatial temperature distribution or the 'reactive volume' around the plasma.

- At low pressures (< 200 mbar), when plasma is in a hybrid contraction state [9], preheating adversely affects performance by decreasing the radial temperature profile (reactive area) and axial plasma profile, resulting in a reduced reactive volume, which correlates to reduced conversion.
- At higher pressures (> 300 mbar), when the plasma is fully contracted, preheating demonstrates substantial benefits by expanding the spatial temperature profile, or the reactive volume, which relates to improved conversion.

For example, at 700 mbar under constant $P_{MW} = 1000$ W, preheating to 700 K increases conversion by ~1.7 times compared to baseline conditions, which correlates directly with an increase in the reactive area of ~1.5 times. Similar improvements were observed at 900 mbar with only 500 K preheating. Furthermore, the expanded reactive volume observed with preheating modifies the reactive volume-bulk gas interface, creating a larger region where temperatures exceed the CO_2 dissociation threshold (> 1500 K). The spectroscopic measurements reveal that preheating primarily affects the spatial distribution of thermal energy rather than core plasma properties, as the core plasma temperature was consistently reported to be between ~6000–7000 K, regardless of T_{inlet}, while peripheral temperatures remained below ~1000 K, maintaining effective quenching capability. This suggests that the classical description of thermal instability-driven contraction should be expanded to include upstream flow considerations, particularly with the interplay between convective cooling, temperature gradients, and reactive volume formation. The pressure-dependent response to preheating reveals that gas density and flow dynamics play critical roles in determining the spatial temperature distribution beyond what electron density alone would predict. This means that the high-temperature reactive volume, in which CO_2 dissociation is dominated, is not limited to the plasma volume as defined by the electronically excited atomic oxygen 777 nm emission.

Moreover, the relationship between preheating and performance follows a non-linear pattern. At higher power conditions ($P_{total} = 1500$ W), conversion at 900 mbar shows a decline at higher T_{inlet} (850 K), suggesting that 850 K is above the optimal temperature range. Thermographic imaging revealed a downward shift in peak wall temperature with increasing T_{inlet} and enhanced thermal losses through the walls that correlate directly to reduced conversion as a result of accelerated recombination processes in the downstream region. The increased wall losses and evidence of enhanced recombination suggest that implementing effective downstream quenching strategies, such as effluent nozzles, could further improve overall system performance by mitigating product loss. This highlights the critical role of upstream thermal management in determining downstream conversion, providing a theoretical foundation for optimizing plasma-chemical processes through strategic heat distribution rather than increased power input.

Our findings demonstrate that recycling even small amounts of the input power (< 14 %) for preheating can significantly improve energy efficiency and conversion, showing that strategic implementation of heat recovery from downstream processes could substantially improve

overall system efficiency in industrial applications. The observed pressure-dependent effects also indicate that preheating, if optimized, could extend high energy efficiency operation into the near-atmospheric pressure regime, reducing pumping power requirements. A comprehensive understanding of these aspects will be crucial for translating the observed benefits of preheating into practical improvements for industrial MW plasma-based CO_2 conversion, ultimately contributing to the development of sustainable technologies for carbon utilization and renewable energy storage.

CRediT authorship contribution statement

E.R. Mercer: Writing – original draft, Visualization, Software, Methodology, Investigation, Formal analysis, Data curation, Conceptualization. **C.F.A.M. van Deursen:** Writing – original draft, Visualization, Software, Methodology, Investigation, Formal analysis. **F.J.J. Peeters:** Writing – review & editing, Validation, Supervision, Software, Methodology, Conceptualization. **W.A. Bongers:** Writing – review & editing, Supervision, Resources, Funding acquisition. **F.M.A. Smits:** Writing – review & editing, Supervision, Resources. **M.C.M. van de Sanden:** Writing – review & editing, Supervision, Resources, Funding acquisition. **A. Bogaerts:** Writing – review & editing, Supervision, Resources, Funding acquisition.

Funding sources

This research was partially supported by the European Research Council (ERC) under the European Union's Horizon 2020 research and innovation program (grant agreement No 810182 – SCOPE ERC Synergy project), as well as partially supported by The Dutch Research Council (NWO) Open Technology Programme (grant agreement No 18978, TECH).

Declaration of competing interest

The authors declare that they have no known competing financial interests or personal relationships that could have appeared to influence the work reported in this paper.

Acknowledgements

The work presented in this manuscript represents the culmination of five years of research, during which many individuals played crucial roles in bringing this project to fruition. We extend our sincere gratitude to all those who provided their active support throughout this journey. The authors would like to acknowledge the exceptional contributions from the entire support staff at DIFFER. Special thanks go to our dedicated technicians, Martijn and Aron, whose expertise and assistance were invaluable. We are equally grateful to the electrical department and drawing room staff for their technical guidance and creative solutions that helped us overcome numerous challenges. We wish to express our appreciation to the machine shop for their extraordinary craftsmanship, precision, and dedication. Their skill and commitment to transforming our designs into functional experimental components was fundamental to the success of this research, without which this work would not have been possible. Finally, we thank our academic collaborators and the leadership at DIFFER for fostering an environment that encourages innovation and interdisciplinary research in the field of plasma physics and sustainable energy technologies.

Appendix A. Supplementary data

Supplementary data to this article can be found online at https://doi.org/10.1016/j.cej.2025.167294.

Data availability

Data will be made available on request.

References

[1] Copernicus Climate Change Service (C3S) (Ed.), Global Climate Highlights 2024 The Annual Climate Summary, 2025.
[2] F.A. D'Isa, E.A.D. Carbone, A. Hecimovic, U. Fantz, Performance analysis of a 2.45 GHz microwave plasma torch for CO2 decomposition in gas swirl configuration, Plasma Sources Sci. Technol. 29 (10) (2020) 105009, https://doi.org/10.1088/1361-6595/abaa84.
[3] A. Hecimovic, F.A. D'Isa, E. Carbone, U. Fantz, Enhancement of CO2 conversion in microwave plasmas using a nozzle in the effluent, J. CO_2 Util. 57 (2022) 101870, https://doi.org/10.1016/j.jcou.2021.101870.
[4] A. van de Steeg, P. Viegas, A. Silva, T. Butterworth, A. van Bavel, J. Smits, P. Diomede, M. van de Sanden, G. van Rooij, Redefining the microwave plasma-mediated CO2 reduction efficiency limit: the role of O–CO2 association, ACS Energy Lett. 6 (8) (2021) 2876–2881.
[5] C. van Deursen, H. Van Poyer, W. Bongers, F. Peeters, F. Smits, M. van de Sanden, Effluent nozzles in reverse-vortex-stabilized microwave CO2 plasmas for improved energy efficiency, J CO_2 Util 88 (2024) 102952.
[6] E.R. Mercer, S. Van Alphen, C.F.A.M. van Deursen, T.W.H. Righart, W.A. Bongers, R. Snyders, A. Bogaerts, M.C.M. van de Sanden, F.J.J. Peeters, Post-plasma quenching to improve conversion and energy efficiency in a CO2 microwave plasma, Fuel 334 (2023) 126734, https://doi.org/10.1016/j.fuel.2022.126734.
[7] W. Bongers, H. Bouwmeester, B. Wolf, F. Peeters, S. Welzel, D. van den Bekerom, N. den Harder, A. Goede, M. Graswinckel, P.W. Groen, Plasma-driven dissociation of CO2 for fuel synthesis, Plasma Process. Polym. 14 (6) (2017) 1600126.
[8] E. Carbone, F. D'Isa, A. Hecimovic, U. Fantz, Analysis of the C2 (d3Πg-a3Πu) Swan bands as a thermometric probe in CO2 microwave plasmas, Plasma Sources Sci. Technol. (2019), https://doi.org/10.1088/1361-6595/ab74b4.
[9] A.J. Wolf, T.W. Righart, F. Peeters, W. Bongers, Van DeM. Sanden, Implications of thermo-chemical instability on the contracted modes in CO2 microwave plasmas, Plasma Sources Sci. Technol. 29 (2) (2020) 025005.
[10] D.C.M. van den Bekerom, J.M.P. Linares, T. Verreycken, E.M. van Veldhuizen, S. Nijdam, G. Berden, W.A. Bongers, M.C.M. van de Sanden, G.J. van Rooij, The importance of thermal dissociation in CO2 microwave discharges investigated by power pulsing and rotational Raman scattering, Plasma Sources Science and Technology 28 (5) (2019) 055015, https://doi.org/10.1088/1361-6595/aaf519.
[11] L. Vialetto, A.W. van de Steeg, P. Viegas, S. Longo, G.J. van Rooij, M.C.M. van de Sanden, J. van Dijk, P. Diomede, Charged particle kinetics and gas heating in CO2 microwave plasma contraction: comparisons of simulations and experiments, Plasma Sources Sci. Technol. 31 (5) (2022) 055005, https://doi.org/10.1088/1361-6595/ac56c5.
[12] J. Li, X. Zhang, J. Shen, T. Ran, P. Chen, Y. Yin, Dissociation of CO2 by thermal plasma with contracting nozzle quenching, J CO_2 Util 21 (2017) 72–76, https://doi.org/10.1016/j.jcou.2017.04.003.
[13] A. Van de Steeg, L. Vialetto, A.S. d. Silva, P. Viegas, P. Diomede, M. Van de Sanden, G. Van Rooij, The chemical origins of plasma contraction and thermalization in CO2 microwave discharges, J. Phys. Chem. Lett. 13 (5) (2022) 1203–1208.
[14] A.J. Wolf, F. Peeters, P. Groen, W. Bongers, Van DeM. Sanden, CO2 conversion in nonuniform discharges: disentangling dissociation and recombination mechanisms, J. Phys. Chem. C 124 (31) (2020) 16806–16819.
[15] J.H.O. Schönherr, in: U.S.P. Office (Ed.), Production of Long Stable Electric Arcs, 1909. Germany.
[16] The manufacture of nitrates from the atmosphere, Nature 89 (2227) (1912) 463–465, https://doi.org/10.1038/089463a0.
[17] K.H.R. Rouwenhorst, F. Jardali, A. Bogaerts, L. Lefferts, From the Birkeland–Eyde process towards energy-efficient plasma-based NOX synthesis: a techno-economic analysis, Energy Environ. Sci. 14 (5) (2021) 2520–2534, https://doi.org/10.1039/D0EE03763J.
[18] M.I. Boulos, Handbook of Thermal Plasmas, Springer Nature, Switzerland, 2023, https://doi.org/10.1007/978-3-030-84936-8.
[19] L. Kerker, R. Müller, Plasma reforming process for the production of reducing gases, Stahl Eisen 104 (22) (1984). Germany, Federal Republic of).
[20] B. Cárdenas, S.D. Garvey, B. Kantharaj, M.C. Simpson, Gas-to-gas heat exchanger design for high performance thermal energy storage, J Energy Storage 14 (2017) 311–321, https://doi.org/10.1016/j.est.2017.03.004.
[21] S.B. Shenoy, A. Rabinovich, A. Fridman, H. Pearlman, Process optimization of methane reforming to syngas using gliding arc plasmatron, Plasma Process. Polym. 16 (4) (2019) 1800159, https://doi.org/10.1002/ppap.201800159.
[22] C. Hyun Cho, J.H. Kim, J.K. Yang, I.S. Park, Y.-S. Choi, I.J. Kang, Dry reforming process using microwave plasma generator with high carbon dioxide conversion efficiency for syngas production, Fuel 361 (2024) 130707, https://doi.org/10.1016/j.fuel.2023.130707.
[23] S. Jo, D.H. Lee, Y.-H. Song, Effect of gas temperature on partial oxidation of methane in plasma reforming, Int. J. Hydrogen Energy 38 (31) (2013) 13643–13648, https://doi.org/10.1016/j.ijhydene.2013.08.049.
[24] A.J. Wolf, T.W.H. Righart, F.J.J. Peeters, P.W.C. Groen, M.C.M. van de Sanden, W. A. Bongers, Characterization of CO2 microwave plasma based on the phenomenon of skin-depth-limited contraction, Plasma Sources Science and Technology 28 (11) (2019) 115022, https://doi.org/10.1088/1361-6595/ab4e61.

[25] G. Raposo, A.W. van de Steeg, E.R. Mercer, C.F.A.M. van Deursen, H.J. L. Hendrickx, W.A. Bongers, G.J. van Rooij, M.C.M. van de Sanden, F.J.J. Peeters, Flame bands: CO + O chemiluminescence as a measure of gas temperature, J. Phys. D Appl. Phys. 54 (37) (2021) 374005, https://doi.org/10.1088/1361-6463/ac0924.

[26] B. Wanten, R. Vertongen, R. De Meyer, A. Bogaerts, Plasma-based CO2 conversion: How to correctly analyze the performance? J. Energy Chem. 86 (2023) 180–196, https://doi.org/10.1016/j.jechem.2023.07.005.

[27] P. Viegas, L. Vialetto, A.J. Wolf, F.J.J. Peeters, P.W.C. Groen, T.W.H. Righart, W. A. Bongers, M.C.M. van de Sanden, P. Diomede, Insight into contraction dynamics of microwave plasmas for CO2 conversion from plasma chemistry modelling, Plasma Sources Science and Technology 29 (10) (2020) 105014, https://doi.org/10.1088/1361-6595/abb41c.

[28] O. Biondo, A. Hughes, A. van de Steeg, S. Maerivoet, B. Loenders, G. van Rooij, A. Bogaerts, Power concentration determined by thermodynamic properties in complex gas mixtures: the case of plasma-based dry reforming of methane, Plasma Sources Science and Technology 32 (4) (2023) 045001, https://doi.org/10.1088/1361-6595/acc6ec.

[29] L. Vialetto, Modelling of plasma for CO2 conversion: electron kinetics, chemistry and transport, 2021.

[30] C.K. Kiefer, R. Antunes, A. Hecimovic, A. Meindl, U. Fantz, CO2 dissociation using a lab-scale microwave plasma torch: An experimental study in view of industrial application, Chem. Eng. J. 481 (2024) 148326, https://doi.org/10.1016/j.cej.2023.148326.

[31] K. Wang, S. Ceulemans, H. Zhang, I. Tsonev, Y. Zhang, Y. Long, M. Fang, X. Li, J. Yan, A. Bogaerts, Inhibiting recombination to improve the performance of plasma-based CO2 conversion, Chem. Eng. J. 481 (2024) 148684, https://doi.org/10.1016/j.cej.2024.148684.

[32] R. Vertongen, G. Trenchev, R. Van Loenhout, A. Bogaerts, Enhancing CO2 conversion with plasma reactors in series and O2 removal, J CO_2 Util 66 (2022) 102252, https://doi.org/10.1016/j.jcou.2022.102252.